Research Article Vol. 13, No. 8 / 1 Aug 2023 / Optical Materials Express 2426
Optical Materials EXPRESS

Effect of molecular concentration on excitonic nanostructure based refractive index sensing and near-field enhanced spectroscopy

ARPAN DUTTA[1,2,3] AND J. JUSSI TOPPARI[1,4]

[1]Nanoscience Center and Department of Physics, University of Jyväskylä, P.O. Box 35, FI-40014, Finland
[2]Currently with Department of Mechanical and Materials Engineering, University of Turku, FI-20014, Finland
[3]arpan.dutta@utu.fi
[4]j.jussi.toppari@jyu.fi

Abstract: Organic thin film based excitonic nanostructures are of great interest in modern resonant nanophotonics as a promising alternative for plasmonic systems. Such nanostructures sustain propagating and localized surface exciton modes that can be exploited in refractive index sensing and near-field enhanced spectroscopy. To realize these surface excitonic modes and to enhance their optical performance, the concentration of the excitonic molecules present in the organic thin film has to be quite high so that a large oscillator strength can be achieved. Unfortunately, this often results in a broadening of the material response, which might prevent achieving the very goal. Therefore, systematic and in-depth studies are needed on the molecular concentration dependence of the surface excitonic modes to acquire optimal performance from them. Here, we study the effect of molecular concentration in terms of oscillator strength and Lorentzian broadening on various surface excitonic modes when employed in sensing and spectroscopy. The optical performance of the modes is evaluated in terms of sensing, like sensitivity and figure of merit, as well as near-field enhancement, like enhancement factor and field confinement. Our numerical investigation reveals that, in general, an increase in oscillator strength enhances the performance of the surface excitonic modes while a broadening degrades that as a counteracting effect. Most of all, this demonstrates that the optical performance of an excitonic system is tunable via molecular concentration unlike the plasmonic systems. Moreover, different surface excitonic modes show different degrees of tunability and equivalency in performance when compared to plasmons in metals (silver and gold). Our findings provide crucial information for developing and optimizing novel excitonic nanodevices for contemporary organic nanophotonics.

1. Introduction

Interaction of light with metallic nanostructures can excite a collective oscillation of the metal's conduction electrons, also known as plasmons. The excited plasmonic modes can be spectroscopically resolvable in the optical response of the metallic system and usually involve a strongly enhanced electromagnetic near-field around the structure [1–3]. Depending on the type of the nanostructure, different plasmonic modes can be excited such as surface plasmon polariton (SPP) at the interface of a flat metal film and a dielectric material [4], localized surface plasmon (LSP) in a metal nanoparticle (NP) [5], and plasmonic surface lattice resonance (PSLR) in a periodic structure, e.g., an array of metal NPs [6].

Plasmonic modes are extremely sensitive to the dielectric constant of their surrounding medium and even a slightest change in the refractive index (RI) of the host medium can significantly shift

#497366 https://doi.org/10.1364/OME.497366
Journal © 2023 Received 8 Jun 2023; revised 19 Jul 2023; accepted 19 Jul 2023; published 31 Jul 2023

Optical Materials EXPRESS

the spectral position of the SPP [7], LSP [8], and PSLR [9] modes. Such feature enables the application of nanoplasmonic structures in the development of RI sensors [5,7–11].

Plasmonic modes (SPP, LSP, and PSLR) can also provide enhancement [12–15] and confinement [16–18] of light at the near-field close to the structure. Consequently, metallic nanostructures are widely exploited as resonant substrates for near-field enhanced spectroscopy ranging from weak [19–22] to strong [23–25] light-matter coupling.

The origin of the plasmonic properties in metals can be explained in terms of the real part of their complex and dispersive dielectric function ($Re\{\epsilon\}$) [1–3,26,27]. The SPP mode can be supported by a flat metal film in the spectral region where $Re\{\epsilon\} < -1$ while manifestation of LSP mode in a metal NP is only possible in the spectral regime where $Re\{\epsilon\} < -2$ [27]. In the case of noble metals like gold and silver, the negative $Re\{\epsilon\}$ regime, i.e., the spectral regime where $Re\{\epsilon\} < -1$ or -2, covers a major part of the visible spectrum, making them a popular choice in nanoplasmonics [28,29].

Despite the fact that plasmonic materials show unique optical properties ranging from ultraviolet to infrared wavelengths, their performance is often hindered due to the absorption losses, and their fabrication might become complex and expensive. Consequently, a quest emerges for alternative materials which can provide a plasmon-like negative $Re\{\epsilon\}$ regime, especially in the visible range, while exhibiting less losses as well as being somewhat simpler and inexpensive to fabricate compared to the metallic nanostructures. One important class of such materials is highly concentrated organic thin films possessing Frenkel excitons which induce a negative $Re\{\epsilon\}$ regime spectrally located very close to their strong excitonic absorption band [26,27]. Such excitonic materials can support surface exciton polariton (SEP) at an interface of an excitonic film and a dielectric material [26,27,30,31], localized surface exciton (LSE) in an excitonic NP [27,32,33], and excitonic surface lattice resonance (ESLR) in a periodic array of excitonic NPs [34]. The SEP, LSE, and ESLR modes are analogous to the SPP, LSP, and PSLR modes, respectively. Eventually, like the plasmonic modes, these surface excitonic modes show sensitivity towards the surrounding dielectric environment [31] and provide enhancement as well as confinement of the near-field [35]. Hence, excitonic nanostructures possessing these modes can be a potential alternative for the plasmonic systems in RI sensing and in near-field enhanced spectroscopy.

The optical responses associated with the aforementioned plasmonic and excitonic modes might appear analogous but the underlying physical mechanism in those systems differs fundamentally. The plasmonic resonances originate from the presence of free conduction electrons in metals which in the simplest case can be described by the Drude model. Contrastingly, the excitonic modes in the organic thin films appear due to the Frenkel excitons which can be expressed by the Lorentz oscillator model [27]. Unlike Drude metals, the complex permittivity (ϵ) of an excitonic material is directly proportional to the Lorentz oscillator strength (f) and the Lorentz linewidth (γ) of the material absorption [36,37] which scales with the molecular concentration [27,32,33,38]. An increase in molecular concentration usually results in a rise in molecular absorption accompanied with a linewidth broadening, which accounts for a simultaneous rise in the magnitude of f and γ [36,37]. Such rise in f and γ can directly affect the magnitude of $Re\{\epsilon\}$ and thereby, the negative $Re\{\epsilon\}$ regime. As a consequence, the surface excitonic modes exhibit modification in their strength and light coupling efficiency [26,27,39,40]. Therefore, optical performance of the surface excitonic modes can be tuned by varying the concentration of the excitonic molecules.

In this work, we investigate the effect of the molecular concentration (in terms of f and γ) on the performance of excitonic nanostructures when used for RI sensing and near-field enhanced spectroscopy. The J-aggregate of cyanine dye (TDBC) is considered as the excitonic molecule doped in a polyvinyl alcohol (PVA) matrix. Three kinds of excitonic nanostructures are studied, as shown in Fig. 1 - (i) a TDBC-PVA thin film which supports SEP under excitation in the Kretschmann configuration (Fig. 1(a)), (ii) a TDBC-PVA nanosphere which possesses LSE

Optical Materials EXPRESS

(Fig. 1(b)), and (iii) a square lattice of TDBC-PVA nanospheres manifesting ESLR (Fig. 1(c)). In all cases, the sensing performance is evaluated in terms of sensitivity and a commonly used figure of merit for RI sensing, i.e. the sensitivity divided by the width of the utilized spectral resonance, while the assessment in spectroscopy is based on the near-field intensity enhancement (NFIE), Purcell enhancement, and field-confinement. Our numerical findings show that the performance parameters (sensitivity, figure of merit, NFIE, Purcell enhancement, and field-confinement) of a surface excitonic mode can be tuned efficiently by varying the molecular concentration. Moreover, SEP, LSE, and ESLR based nanostructures provide different degrees of tunability when concentration is varied. Our comprehensive study on different types of surface excitonic modes with varying concentration provides key information for developing and optimizing novel organic material based excitonic nanodevices for sensing and spectroscopy.

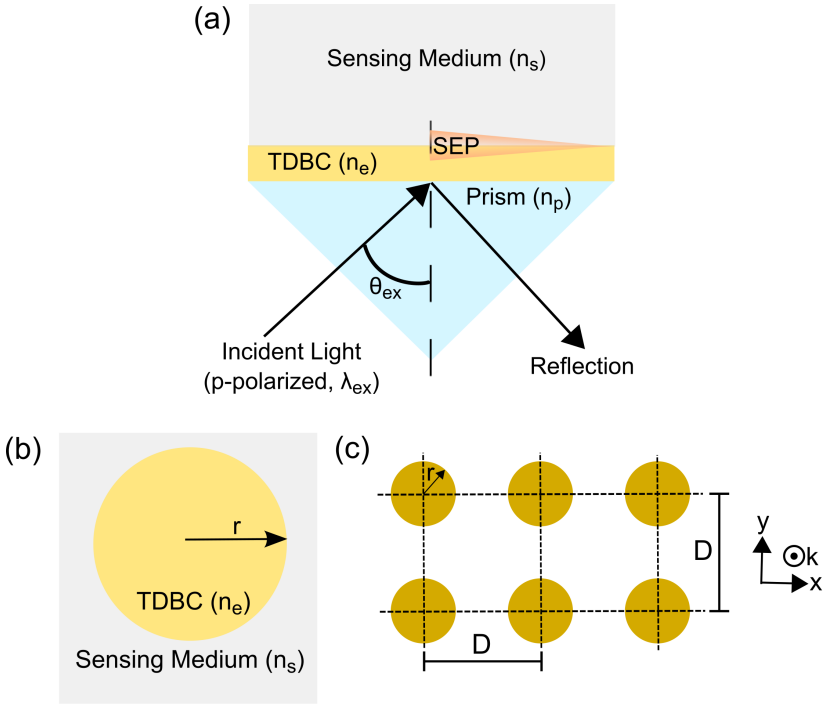

Fig. 1. (a) A TDBC-PVA thin film supporting SEP under excitation in the Kretschmann configuration. (b) A TDBC-PVA nanosphere possessing LSE. (c) A square lattice of TDBC-PVA nanospheres manifesting ESLR.

2. Negative $Re\{\epsilon\}$ regime

Before analyzing the performance of different excitonic systems it is important to determine their negative $Re\{\epsilon\}$ regime as a function of molecular concentration. To do so, we evaluate the spectral regime where $Re\{\epsilon\} < -1$ or -2 as a function of Lorentz oscillator strength (f) and Lorentz linewidth (γ). The complex and dispersive dielectric function (ϵ) of an excitonic material like our TDBC-PVA system can be estimated using the Lorentz oscillator model (LOM) [27,37,41] as

$$\epsilon(E) = \epsilon_\infty + \frac{fE_0^2}{(E_0^2 - E^2 - i\gamma E)}, \tag{1}$$

Optical Materials EXPRESS

where E is the energy, ϵ_∞ is the dielectric constant of the host polymer (i.e. PVA), f is the oscillator strength of the excitonic absorption having E_0 as its spectral peak position and γ as its spectral linewidth [27,37,41]. To model TDBC, we choose realistic values for LOM parameters taken from the existing experimental studies [27,41–44]. In Eq. (1), we consider $\epsilon_\infty = 2.1025$ [41] and $E_0 = 2.08$ eV [41], while f and γ are treated as variables. In the Refs. [27,41–44], γ varies from 0.025 eV to 0.12 eV and f varies from 0.05 to 0.51. In line with this realistic parameter range, we vary γ from 0.05 eV to 0.15 eV while the range of f (0.05 to 0.9) is extended upwards to see whether a possible increase in the absorption beyond the already achieved values could bring extra improvements.

An increase in molecular concentration results in an increase in molecular absorption usually accompanied with a linewidth broadening accounting for a simultaneous rise in f and γ [36,37,44]. We used an experimental study on TDBC [44] to extract γ as a function of f. The γ values are directly from the study while the values for f were obtained by fitting the absorption data (see Fig. 7(a) in Appendix). The details of the fitting method can be found in our earlier work [37]. The correlation between f and γ is plotted in Appendix in Fig. 7(b) where all the values are within the realistic ranges discussed above. It should be noted here that this is a correlation extracted from a single study and thus, not the only possible relation. The aggregation of molecules and thus, the broadening (γ) depends on many different factors (e.g., fabrication process) and can vary a lot. Thus, we need to study wider range of parameter combinations and keep this as a guiding example of the interdependence of the parameters.

To model the above, we calculate real ($Re\{\epsilon\}$) and imaginary ($Im\{\epsilon\}$) parts of the dielectric function (ϵ) of a 60 nm thick TDBC-PVA layer using Eq. (1) with varying f and γ. The curves are shown in Fig. 2(a). The associated absorption is calculated using transfer-matrix method (TMM) [45,46] implemented in MATLAB [47,48], similarly as in our earlier studies [37].

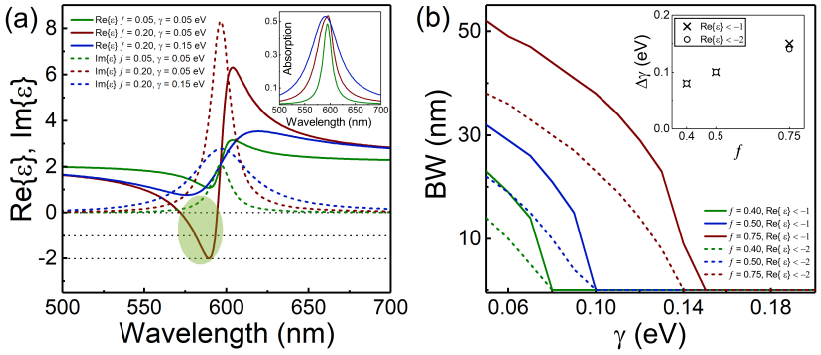

Fig. 2. (a) The real ($Re\{\epsilon\}$, solid curves) and imaginary ($Im\{\epsilon\}$, dashed curves) parts of the dielectric function (ϵ) of a 60 nm thick TDBC-PVA layer calculated using Eq. (1) for different values of Lorentz oscillator strength (f) and Lorentz linewidth (γ). Here, $\epsilon_\infty = 2.1025$ and $E_0 = 2.08$ eV as discussed in the text. The corresponding absorption spectra (in matching colors) computed by TMM are shown in the inset. The green spot on the figure depicts the region where $Re\{\epsilon\}<0$ and $|Im\{\epsilon\}|<|Re\{\epsilon\}|$ for the red curves. (b) Bandwidth (BW) of surface excitonic modes for different values of f and γ. In the inset, the broadening tolerance ($\Delta\gamma$) is plotted as a function of f.

The green curves in Fig. 2(a) represent $Re\{\epsilon\}$ (solid) and $Im\{\epsilon\}$ (dashed) of our *pristine* TDBC-PVA film with $f = 0.05$ and $\gamma = 0.05$ eV. The corresponding absorption is shown in the inset of Fig. 2(a) (green curve). It is clear from the figure that our *pristine* layer is unable to support any surface excitonic mode since its $Re\{\epsilon\}$ is positive in the wavelength region of interest (500-700 nm). To address a rise in concentration, we first increase f to 0.20 while keeping γ at

Optical Materials EXPRESS

0.05 eV. The red curves in Fig. 2(a) depict the case with the corresponding absorption with the same color in the inset. Clearly now $Re\{\epsilon\}$ becomes negative (almost −2) indicating that our TDBC layer can support the surface excitonic modes in a narrow spectral window (~ 575 – 595 nm) at the blue side of the molecular absorption peak (~ 600 nm). However, to realize the actual effect of a rising concentration one should increase both f and γ simultaneously. The blue curves in Fig. 2(a) show the case (with the related absorption in the inset) where f is kept at 0.20 and γ rises from 0.05 eV to 0.15 eV. Clearly, the increase in γ counteracts the effect seen for the sole rise in only f by making $Re\{\epsilon\}$ positive again like in the *pristine* case, and eventually, no surface excitonic mode can be supported by the TDBC layer.

To develop more insight on this counteracting behaviour we calculate the spectral regions where $Re\{\epsilon\}<-1$ and $Re\{\epsilon\}<-2$, reported in Fig. 8 in Appendix, for different values of f and γ. To ensure minimal material loss, we also impose an additional condition, i.e., $|Im\{\epsilon\}|<|Re\{\epsilon\}|$ [40], for our reported spectral region. The bandwidth (BW) for the possible existence of the surface excitonic modes is evaluated as the difference between the upper and the lower boundaries of the aforementioned spectral regions (see Fig. 8 in Appendix). The solid curves in Fig. 2(b) report the BW of SEP mode ($Re\{\epsilon\}<-1$) while the dashed curves report the same for LSE and ESLR mode ($Re\{\epsilon\}<-2$).

In Fig. 2(b), the BW values at the vertical axis, i.e., at $\gamma = 0.05$ eV, present the scenario where the BW is increasing with increasing f, i.e., $f = 0.40$ (green) to $f = 0.75$ (red) via $f = 0.50$ (blue), considering a constant γ (no broadening). However, when the broadening is incorporated, i.e., γ increases from 0.05 eV to 0.20 eV for a constant value of f (0.40 or 0.50 or 0.75), in all cases, the BW drops drastically and vanishes after a certain value of γ as one can see in Fig. 2(b). This finding clearly indicates that when both f and γ increase, as usually happens when increasing the film concentration [36,37,44], they counteract each other's effects.

As seen from Fig. 2(b), for all f there always exists a maximum γ, after which the surface excitonic mode is no more possible, because there is no more spectral region with $Re\{\epsilon\}<-1$ or $Re\{\epsilon\}<-2$, i.e., BW= 0. For example, for $f = 0.5$ this value is $\gamma = 0.1$ eV (blue curve). This range (e.g., $\gamma \in [0, 0.1]$ eV for $f = 0.5$) can be considered as a broadening tolerance, $\Delta\gamma(f)$, of a surface excitonic mode since at any $\gamma<\Delta\gamma$ the mode is always allowed at some spectral region, but for $\gamma>\Delta\gamma$ it vanishes in all frequencies. The evolution of $\Delta\gamma(f)$ as a function of f is plotted in the inset of Fig. 2(b) and it is clear from the figure that the higher the f, the larger the $\Delta\gamma$. This is an important finding since it can provide a solution to mitigate the above-mentioned counteracting problem while increasing the molecular concentration. By increasing the molecular concentration one can increase f which will push the magnitude of $\Delta\gamma$ to better tolerate the inevitable linewidth broadening. However, care has to be taken in choosing the molecule, so that γ will not increase too much while increasing the concentration and f.

3. Surface exciton polariton

After establishing the initial conditions as well as the spectral range where TDBC-PVA system can support the surface excitonic modes, we first focus on SEP mode under the Kretschmann configuration [30,31]. The SEP mode can be excited in a multilayer system such as air/TDBC-PVA thin film/prism structure where the p-polarized incident light is coupled through the prism. The air can be replaced by the sensing medium for sensing application [31] and by the analyte for spectroscopy [23,36]. The schematic of such SEP based system is presented in Fig. 1(a). We use the Fresnel multilayer reflection theory [7,49,50] implemented in MATLAB for calculating the reflectivity (R) of the system since SEP mode is manifested as a dip in the attenuated total reflection (ATR) spectrum [50]. The RI of the prism (n_p) is considered as 1.50 which corresponds to the common BK7 glass in practice [7]. The RI of the sensing medium (n_s) is varied from 1 to 1.01 with a step size of 0.001 to evaluate the performance of the sensor. The RI of the TDBC-PVA film is obtained as $n_e = \sqrt{\epsilon}$ [51], where ϵ is calculated using Eq. (1).

Optical Materials EXPRESS

We excite the SEP mode supported by a 60 nm thick TDBC-PVA film ($f = 0.5$ and $\gamma = 0.05$ eV) using the Kretschmann configuration in two ways. In the angular scheme we use the p-polarized monochromatic light of wavelength λ_{ex} to excite the system over a broad range of incident angles higher than the critical angle of total internal reflection ($\sim 42^\circ - 90^\circ$). The angle-dependent reflectivity is presented in Fig. 3(a) (blue curve) for $\lambda_{ex} = 569$ nm. The dip found in the reflection profile is the signature of the excited SEP mode. In the spectral scheme, we excite the system by a broadband source (p-polarized white light) at a fixed incident angle (θ_{ex}) and the reflectivity is computed over a wide spectral range. The wavelength-dependent reflectivity is depicted in Fig. 3(a) (red curve) for $\theta_{ex} = 54^\circ$. Similar to the angular case, profound presence of the SEP mode is found as a dip in the spectral reflectance.

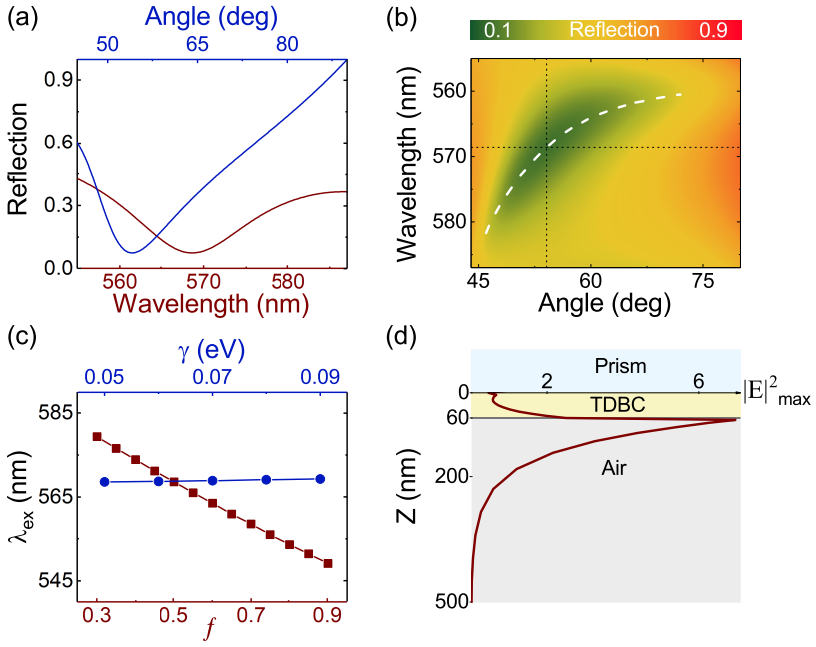

Fig. 3. (a) Angular (excited at $\lambda_{ex} = 569$ nm) and spectral (excited at $\theta_{ex} = 54^\circ$) reflectance of a 60 nm thick TDBC-PVA film ($f = 0.5$ and $\gamma = 0.05$ eV) under Kretschmann configuration. (b) Reflectance of the same film as a contour map where the white dashed curve shows the dispersion of the SEP mode and the black dotted lines show the optimal excitation conditions with minimal reflectance $R(\theta_{ex}, \lambda_{ex})$. (c) Evolution of the optimal excitation wavelength (λ_{ex}) as a function of f and γ. The value of f is varied when $\gamma = 0.05$ eV and the value of γ is varied when $f = 0.5$. (d) FDTD simulated near-field intensity profile of SEP mode. In (a) and (c), the blue and red horizontal axes correspond to the blue and red curves, respectively, while in (c), the blue circles and red squares on the curves of corresponding color depict the discrete data points.

To obtain the optimal excitation conditions (i.e. θ_{ex} and λ_{ex}) of the SEP mode, we compute the reflectance $R(\theta_{ex}, \lambda_{ex})$, with all the angles ($42^\circ - 90^\circ$) and wavelengths supporting the SEP, i.e., within the BW discussed in previous section. The results are reported as a contour map in Fig. 3(b). In the figure, the white dashed curve shows the dispersion of the SEP mode following the spectral and angular minima of the reflectance. The optimal excitation angle (θ_{ex}) and wavelength (λ_{ex}) for sensing are evaluated as the position where $R(\theta_{ex}, \lambda_{ex})$ is the minimum of the whole contour map as shown by the black dotted lines in Fig. 3(b).

The excitation conditions can also vary with respect to f and γ since the BW of the SEP mode is concentration-dependent. To address this, we compute the dispersion of the SEP mode for

Optical Materials EXPRESS

different f and γ where the effect of one parameter is studied by keeping the other as constant. To study the effect of f, it is varied from 0.30 to 0.90, as discussed in the previous section (for f<0.3 BW= 0) with a step size of 0.05 while keeping γ = 0.05 eV (no broadening). To study the effect of broadening, γ is varied from 0.05 eV to 0.09 eV (extent of $\Delta\gamma$) with a step size of 0.01 eV while keeping f = 0.5 constant. In both cases, we extract the excitation conditions (θ_{ex} and λ_{ex}) as $R(\theta_{ex}, \lambda_{ex}) = Min[R(\theta, \lambda)]$. The evolution of the excitation wavelength (λ_{ex}) as a function of f (when γ = 0.05 eV) and of γ (when f = 0.5) is illustrated in Fig. 3(c). From the figure it is clear that λ_{ex} is significantly blue-shifted with increasing f when no broadening is allowed (red curve in Fig. 3(c)). This is consistent with our finding in Fig. 8 (see Appendix) where the BW of SEP mode widens only in the blue-wavelength side with increasing f. However, when the broadening is introduced, λ_{ex} experiences a mild red-shift (blue curve in Fig. 3(c)) counteracting the effect of sole rise only in f without broadening. On the other hand, the angle of excitation (θ_{ex}) is almost unaffected ($\approx 54°$) irrespective of whether f or γ is varied (not shown).

Therefore, for each f (when γ = 0.05 eV) or for each γ (when f = 0.5) there will be a corresponding λ_{ex} at which the SEP mode can be optimally excited over a broad range of incident angles in the angular scheme. On the other hand, at $\theta_{ex} \approx 54°$ the SEP mode can be optimally excited over a wide range of wavelengths in the spectral scheme irrespective of the magnitude of f and γ. Furthermore, one can tune the spectral region of excitation (λ_{ex}) by varying f and γ.

The near-field intensity enhancement (NFIE) is a crucial parameter for surface-enhanced spectroscopy and can be calculated as $|E|^2$ where $E = E_{loc}/E_0$ represents the enhanced (electric) near-field (E_{loc}) normalized by the incident field (E_0) [13,18]. We perform finite-difference time-domain (FDTD) [52,53] simulation to calculate the spatial near-field intensity profile of $|E|^2$ for the SEP mode shown in Fig. 3(d). Like SPP, the evanescent nature of the SEP mode can be seen from the figure and it is consistent with the earlier findings [31,40].

The performance of a RI sensor can be quantified in terms of its sensitivity (S) and figure of merit (F). The sensitivity of a SEP sensor is defined in the angular (spectral) domain as the change in the dip angular (spectral) position $\theta_{dip}(\lambda_{dip})$ divided by the change in the refractive index of the sensing medium (Δn_s) causing the change, i.e., $S_{\theta/\lambda} = \Delta(\theta/\lambda)_{dip}/\Delta n_s$. The angular (spectral) figure of merit, F, commonly used in plasmonic sensing is expressed as the angular (spectral) sensitivity divided by the angular (spectral) full-width at half-maximum (FWHM) of the SEP resonance dip, $\Delta\theta(\Delta\lambda)$ in air (n_s = 1), i.e., $F_{\theta/\lambda} = S_{\theta/\lambda}/\Delta(\theta/\lambda)$ [7,9,31]. In practice, the sensitivities (S_θ and S_λ) are calculated as a slope of the calibration curve, i.e., a plot of the reflectance minimum (θ_{dip} in deg and λ_{dip} in nm) as a function of the RI of sensing medium (n_s in refractive index unit or RIU). The slope is extracted from a linear fit on the calibration curve (see Fig. 9(a) in Appendix).

The effect of f and γ on the sensing performance of a SEP-based system can be understood from Fig. 4. From Fig. 4(a) it is clear that both angular sensitivity (S_θ) and figure of merit (F_θ) increase with increasing f when no broadening is considered (γ = 0.05 eV). Similar trend is found in spectral sensitivity (S_λ) and figure of merit (F_λ) as one can see in Fig. 4(c). Along with a rise in both sensitivities (S_θ and S_λ), the FWHM of the SEP mode experiences a narrowing in both angular ($\Delta\theta$) and spectral ($\Delta\lambda$) domains due to a sole rise in f only (see Fig. 9(c) in Appendix) which results in a monotonic increase in the figure of merits (F_θ and F_λ).

Incorporation of broadening, i.e., increasing γ within $\Delta\gamma$ while keeping f = 0.5, results in a drastic drop in S_θ and a mild fall in S_λ as one can see in Figs. 4(b) and 4(d). Moreover, both $\Delta\theta$ and $\Delta\lambda$ increase when the broadening is considered (see Fig. 9(d) in Appendix). As a result, both F_θ and F_λ drop with a sole rise in γ only. Such outcome implies that the performance of a SEP sensor can be tuned by varying its molecular concentration and the broadening counteracts the positive effect of increasing f.

Optical Materials EXPRESS

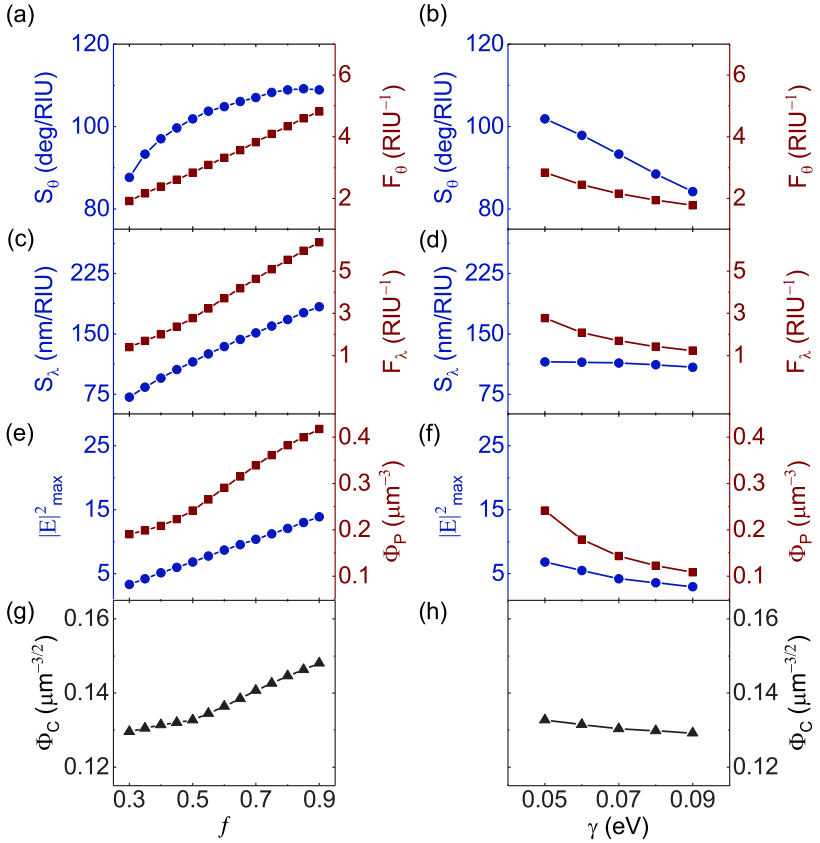

Fig. 4. Performance parameters of the SEP mode supported by a 60 nm thick TDBC-PVA film under the Kretschmann configuration - angular sensitivity (S_θ) and figure of merit (F_θ) as a function of (a) f and (b) γ; spectral sensitivity (S_λ) and figure of merit (F_λ) as a function of (c) f and (d) γ; NFIE maximum ($|E|^2_{max}$) and Purcell enhancement (Φ_P) as a function of (e) f and (f) γ; field-confinement (Φ_C) as a function of (g) f and (h) γ. In the figures in left panel, f is varied when $\gamma = 0.05$ eV, while in right panel, γ is varied within $\Delta\gamma$ when $f = 0.5$. In (a)-(f), the blue and red vertical axes correspond to the blue and red curves, respectively. In all figures, the blue circles, red squares, and black triangles connected by the curves of corresponding color depict the discrete data points.

The performance of our SEP-based system as a resonant platform for near-field enhanced spectroscopy can be determined in terms of NFIE ($|E|^2$), Purcell enhancement, and field-confinement. The NFIE is directly proportional to the electromagnetic enhancement utilized in surface-enhanced spectroscopy [13,18]. The Purcell enhancement for a weak light-matter coupling is the amount of emission enhancement, which is determined by the ratio between the temporal and the spatial confinement of light field [54]. The temporal confinement is defined by the quality factor (Q) while the spatial confinement is determined by the mode volume (V_m), and thus the whole Purcell enhancement is $\Phi_P \propto Q/V_m$ [54,55]. The field-confinement is expressed as $\Phi_C = V_m^{-1/2}$, which is directly proportional to the coupling strength in a single-molecular picture, when the light-matter interaction is strong [17,56].

The effect of f and γ on $|E|^2$, Φ_P, and Φ_C can be seen in Figs. 4(e) to 4(h). We perform FDTD simulations to calculate the distribution of $|E|^2$ and the mode volume (V_m) [57] over a spatial region shown in Fig. 3(d) for different f and γ. In each case, we extract the maximum ($|E|^2_{max}$)

Optical Materials EXPRESS

and the average ($|E|^2_{avg}$) of the NFIE distribution. From Figs. 4(e) and 4(f) it is evident that $|E|^2_{max}$ increases with a rise in f without broadening ($\gamma = 0.05$ eV) while drops when the broadening is considered (at $f = 0.5$). Similar trend is found for $|E|^2_{avg}$ (see Fig. 9(b) in Appendix).

The Purcell enhancement (Φ_P) and field-confinement (Φ_C) improve when Q increases along with a drop in V_m. That happens for increasing f when $\gamma = 0.05$ eV is constant (see Fig. 9(e) in Appendix). Consequently, Φ_P and Φ_C show a monotonic increase as a function of f as shown in Figs. 4(e) and 4(g). In the presence of broadening (at $f = 0.5$), however, Q decreases accompanied with a rise in V_m (see Fig. 9(f) in Appendix). Eventually, Φ_P and Φ_C drop with an increase in γ as depicted in Figs. 4(f) and 4(h). We can infer from such outcomes that efficiency of the SEP mode in confining and enhancing the near-field can be optimized by varying the molecular concentration and like sensing, here also the broadening acts against the positive effect of increasing f.

It is worth to mention here that excitonic thin films possessing SEP mode can be fabricated using solution-based techniques such as spin coating [27] and layer-by-layer deposition [44], which are relatively easy and inexpensive compared to the physical vapor deposition methods typically used to develop metal thin films supporting SPP modes [23,36].

4. Localized surface exciton

After showing that the SEP mode can be exploited for sensing and spectroscopy, and its efficiency can be tuned by the molecular concentration, we next investigate the localized surface exciton (LSE) based system, i.e., a TDBC-PVA nanosphere illustrated in Fig. 1(b). The radius (r) of the nanosphere is taken as 50 nm and the RI of the TDBC-PVA material (n_e) is obtained as $n_e = \sqrt{\epsilon}$ [51], where ϵ is calculated using Eq. (1). The RI of the sensing medium (n_s) is varied again from 1 to 1.01 with a step size of 0.001 to evaluate the performance of the sensor.

The LSE mode of an excitonic NP manifests as a broad peak in its extinction spectrum [27,32,33]. We employ Mie theory [58–62] implemented in MATLAB to compute the extinction efficiency, i.e., the extinction cross-section normalized by the geometrical cross-section, of the nanosphere since its size ($2r = 100$ nm) is beyond the quasi-static limit [63]. In our calculation, the NP is excited by normal incidence of light.

The simulated extinction efficiency (Q_{ext}) in air for the nanosphere with $f = 0.5$ and $\gamma = 0.05$ eV is reported in Fig. 5(a) where the LSE mode is profound as a broad peak around 569 nm. The spatial distribution of NFIE at that wavelength computed by the FDTD method is shown in Fig. 5(b) which resembles a dipolar resonance identical to the particle plasmon mode [64]. The spectral sensitivity (S_λ) and figure of merit (F_λ) of the excitonic nanosphere are calculated using the similar approach used for SEP where $\Delta\lambda$ is now the FWHM of the LSE mode at $n_s = 1$ (air) and λ_{dip} is replaced by the spectral peak position of the LSE mode (λ_{peak}). We track λ_{peak} (≈ 569 nm) as a function of n_s to construct the calibration curve. Then, S_λ is determined as the slope of that curve through a linear fit similar to the case of SEP.

The f-dependent profiles ($\gamma = 0.05$ eV) of the sensing parameters plotted in Fig. 5(c) depict that both S_λ and F_λ monotonically increase with a rise in f, similar to the trend found in the case of SEP. Incorporation of broadening, i.e., varying γ within $\Delta\gamma$ while $f = 0.5$, shows almost no effect on S_λ, however, F_λ drops significantly due to a rise in $\Delta\lambda$ (see Fig. 10 in Appendix), as one can see in Fig. 5(d).

The f- and γ-dependent profiles of $|E|^2$, Φ_P, and Φ_C for the LSE mode can be seen from Figs. 5(e) to 5(h). From the figures it is clear that similar to SEP, $|E|^2_{max}$ and Φ_C increase with rise in f only ($\gamma = 0.05$ eV) while drop when the broadening is incorporated (at $f = 0.5$). Identical trend is found for $|E|^2_{avg}$ while the trend is opposite for V_m (see Fig. 10 in Appendix) which explains the profile of Φ_C. Strikingly, the trend of Φ_P is monotonically decreasing irrespective of the broadening. That is because, unlike in SEP, $\Delta\lambda$ of the LSE mode increases and hence, Q drops regardless of whether f or γ is increasing (see Fig. 10 in Appendix). Based on these findings, we

Optical Materials EXPRESS

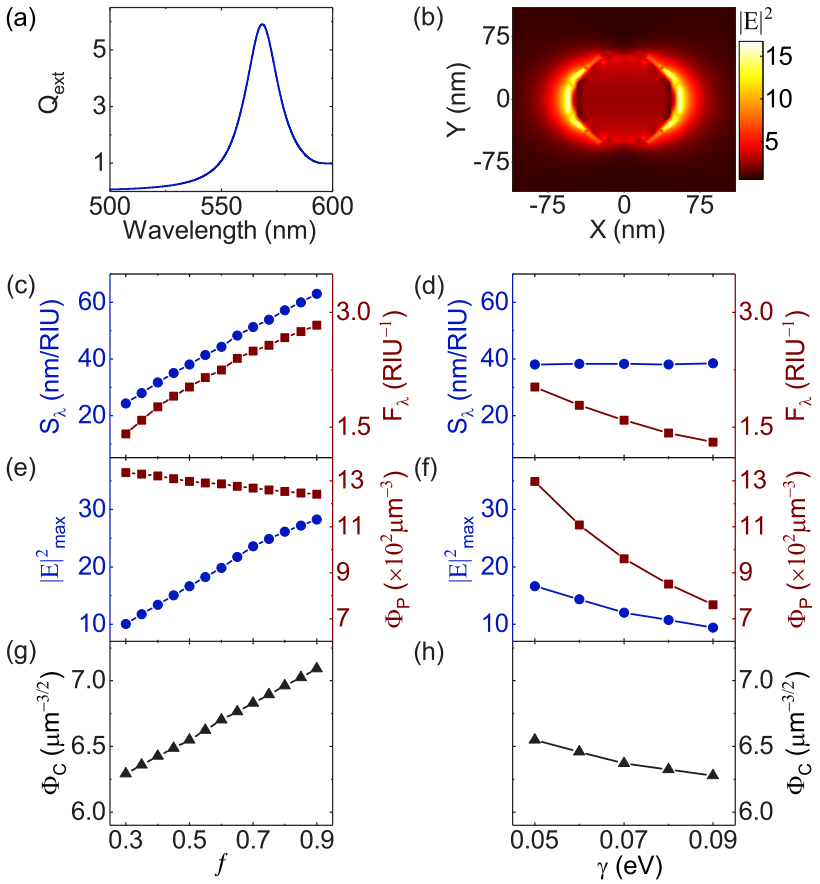

Fig. 5. (a) Extinction efficiency (Q_{ext}) of a TDBC-PVA nanosphere having a diameter of 100 nm, $f = 0.5$, and $\gamma = 0.05$ eV. (b) Spatial distribution of NFIE around the nanosphere in air at its LSE resonance wavelength 569 nm computed by FDTD method. Performance parameters of the LSE mode - spectral sensitivity (S_λ) and figure of merit (F_λ) as a function of (c) f and (d) γ; NFIE maximum ($|E|^2_{max}$) and Purcell enhancement (Φ_P) as a function of (e) f and (f) γ; field-confinement (Φ_C) as a function of (g) f and (h) γ. In the left panel of figures (c)-(h), f is varied when $\gamma = 0.05$ eV, while in the right panel, γ is varied within $\Delta\gamma$ when $f = 0.5$. The blue circles, red squares, and black triangles connected by the curves of corresponding color depict the calculated discrete data points. In (c)-(f), the blue and red vertical axes correspond to the blue and red curves, respectively.

can reckon that like SEP, the performance of the LSE mode in sensing and spectroscopy can also be modified via molecular concentration where the effects of f and γ are mostly counteracting.

It should be noted here that we choose excitonic nanospheres [27,32] as the LSE based system for simplicity and existence of an analytic solution. In practice, any arbitrary-shaped excitonic NP can support the LSE mode in the spectral regime where $Re\{\epsilon\} < -2$ [35,65]. Thus, an LSE based system can be fabricated either as a homogeneous system, e.g., a planar structure by lithographically patterning an excitonic thin film [66], or as a core-shell system, e.g., a dielectric

Optical Materials EXPRESS

NP (core) coated with an excitonic material (shell) [33] using inexpensive chemical synthesis methods [41]. In both cases, one can avoid the expensive physical vapor deposition methods typically used to develop metal NPs supporting LSP modes [13].

5. Excitonic surface lattice resonance

After confirming that both the fundamental surface excitonic modes of the excitonic material are promising as a RI sensor and resonant substrate, we delve into a periodic array of previous NPs possessing excitonic surface lattice resonance (ESLR). The ESLR mode is usually much sharper/narrower and stronger than the dipolar LSE mode present in an isolated NP [9]. To advance this idea, we study a two-dimensional (2D) array (square lattice) of excitonic nanospheres having a well-defined lattice period (D) in both x and y directions as illustrated in Fig. 1(c).

The PSLR mode supported by a metal NP array performs optimally when the mediums above and below the array have identical RI, i.e., the difference between the refractive indices of the substrate and superstrate is very small [9,67,68]. For an excitonic NP array, the same index-matching condition applies and an asymmetric refractive-index environment (a large index mismatch between substrate and superstrate) results in a suppression of the ESLR mode. Keeping that in mind we consider that our designed array is in an index-matched environment having the same RI (n_s) everywhere. In practice, this can be implemented by having the array on a glass substrate with an index-matching oil on top [9,67]. The sensing performance of the array is evaluated by varying n_s similar to the case of SEP and LSE.

The ESLR mode of a NP array manifests as a sharp peak in the extinction spectrum of the array. Such mode can only be excited when the Rayleigh anomaly (or diffraction edge) of the array exists at a higher wavelength than the LSE mode of the individual NPs present in that array [9]. The lattice period (D) of our array is considered as $D = 400$ nm yielding the Rayleigh anomaly around 600 nm which is at a longer wavelength compared to the LSE mode of our individual nanosphere (569 nm). The number of nanospheres (N) included in the array is taken as $N = 400$ resulting in a square lattice of $N \times N$ nanospheres. The extinction profile of our NP array is computed using the coupled dipole (CD) method [34,69–76] implemented in MATLAB. In our computation, the array is excited by normal incidence of light and the nanospheres present in the array are identical with the one discussed in the previous section.

The simulated extinction efficiency (Q_{ext}) of the array is reported in Fig. 6(a) for $f = 0.5$ and $\gamma = 0.05$ eV. The sharp ESLR mode is profound at a wavelength of 606 nm, i.e., higher than the Rayleigh anomaly (600 nm) shown by the dashed vertical line. The spatial distribution of NFIE around each particle at the ESLR wavelength computed by the FDTD method is shown in Fig. 6(b). It clearly depicts a stronger dipole like resonance compared to that of the LSE mode.

The sensing behaviour of our NP array can be understood from Figs. 6(c) and 6(d) where the sensing parameters (S_λ and F_λ) are evaluated using the similar approach employed for the LSE mode. Interestingly, from the figures, one can see that unlike SEP and LSE, S_λ of the ESLR mode increases with both increasing f and γ. However, in both cases, F_λ drops noticeably. That is because, like in LSE, here also $\Delta\lambda$ of the ESLR mode increases along with a drop in Q regardless of whether f or γ is increasing (see Fig. 11 in Appendix).

The f- and γ-dependent profiles of $|E|^2_{max}$ reported in Figs. 6(e) and 6(f), respectively, show an increase in $|E|^2_{max}$ with a sole rise in f only ($\gamma = 0.05$ eV) while a drop when the broadening is incorporated (at $f = 0.5$). The trend is same for $|E|^2_{avg}$ (see Fig. 11 in Appendix) so as for Φ_C as shown in Figs. 6(g) and 6(h) due to a reciprocal trend in V_m (see Fig. 11 in Appendix). Despite that fact, Φ_P shows a decreasing nature due to the same trend in Q as mentioned before irrespective of the broadening. Such findings confirm the dependency of the ESLR mode on molecular concentration and thereby, its tunability considering the counteracting effects of f and γ.

Optical Materials EXPRESS

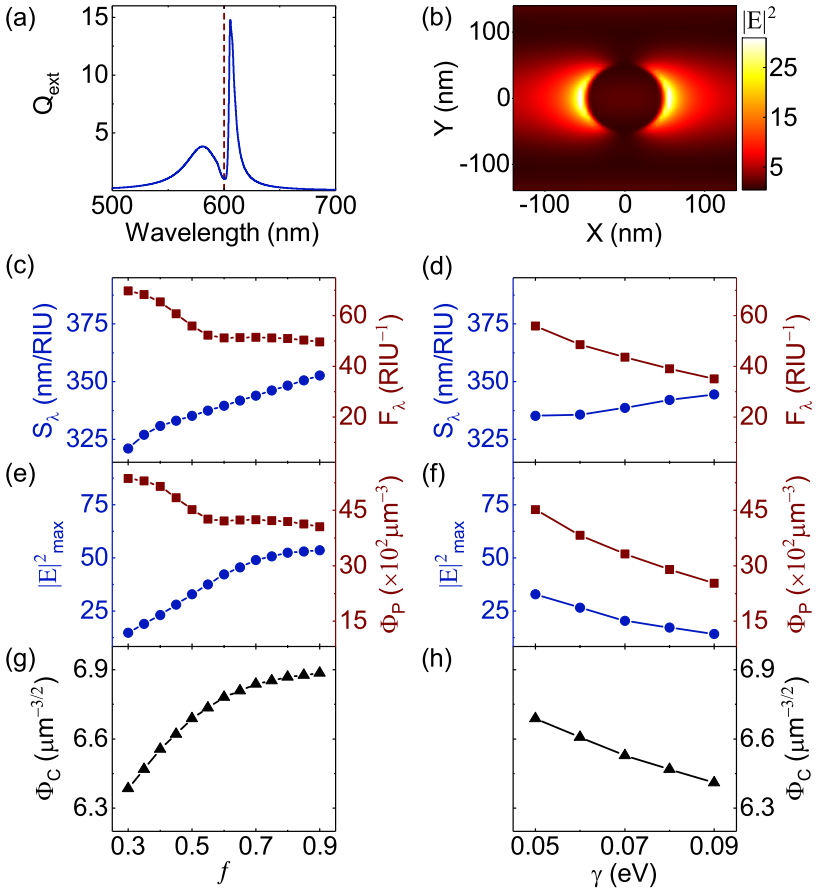

Fig. 6. (a) Extinction efficiency (Q_{ext}) of a 400 × 400 square lattice of TDBC-PVA nanospheres having a diameter of 100 nm and a lattice period of 400 nm with $f = 0.5$ and $\gamma = 0.05$ eV. The vertical dashed line represents the spectral position of the Rayleigh anomaly. (b) Spatial distribution of NFIE around a single particle computed by FDTD method at the wavelength of ESLR. Performance parameters of the ESLR - spectral sensitivity (S_λ) and figure of merit (F_λ) as a function of (c) f and (d) γ; NFIE maximum ($|E|^2_{max}$) and Purcell enhancement (Φ_P) as a function of (e) f and (f) γ; field-confinement (Φ_C) as a function of (g) f and (h) γ. In the left panel of figures (c)-(h), f is varied when $\gamma = 0.05$ eV while in the right panel, γ is varied within $\Delta\gamma$ when $f = 0.5$. The blue circles, red squares, and black triangles connected by the curves of corresponding color depict the calculated discrete data points. In (c)-(f), the blue and red vertical axes correspond to the blue and red curves, respectively.

It is worth to highlight here that like in LSE, we choose arrays of excitonic nanospheres [34] as the ESLR based system for simplicity. Considering the fact, that planar excitonic NPs can also support the surface excitonic modes [35,65], an ESLR based system can be fabricated as a planar NP array (or nano-hole array) by lithographically patterning an excitonic thin film [66]. Like in LSE, here also, one can avoid the expensive metal deposition methods typically used to develop metal NP arrays supporting ESLR modes [67,72].

Optical Materials EXPRESS

6. Comparison with metals

To compare our excitonic systems with their plasmonic analogs, we study similar nanostructures (thin films, nanospheres, and their 2D arrays) made of silver (Ag) and gold (Au) in identical numerical environment. The material models for Ag and Au are taken from existing literature [77]. A detailed comparison in tabular form can be found in Table 1 (see Appendix).

Succinctly, we found that the SEP mode performs comparable or better in angular RI sensing compared to the SPP mode in Au which is consistent with the earlier finding [31]. The LSE mode provides comparable or better electromagnetic enhancement for surface-enhanced spectroscopy than that of the LSP mode in Au which is also inline with the existing literature [35]. Nevertheless, the most surprising and important finding is that all the surface excitonic modes (SEP, LSE, and ESLR) provide comparable (or even better) confinement of light in weak (Φ_P) and strong (Φ_C) coupling regimes compared to their plasmonic counterparts (Ag and Au). Such outcome strongly validates the fact that excitonic nanostructures are a potential alternative for plasmonic systems in RI sensing and enhanced spectroscopy. In our case, TDBC-PVA is a good replacement for Au, however, outperformed by Ag in the visible wavelengths.

7. Conclusion

Concisely, we investigated effect of molecular concentration on excitonic nanostructure based refractive index sensing and near-field enhancement suitable for surface enhanced spectroscopy. Three kinds of excitonic nanostructures were considered - a TDBC-PVA thin film supporting surface exciton polariton (SEP), a TDBC-PVA nanosphere possessing localized surface exciton (LSE), and a square lattice of similar nanospheres manifesting excitonic surface lattice resonance (ESLR). The effect of molecular concentration was studied by varying the oscillator strength (f) and the Lorentzian broadening (γ) of the TDBC-PVA material. The performance in sensing and spectroscopy was evaluated in terms of sensitivity, figure of merit, near-field intensity enhancement, Purcell enhancement, and field confinement. Our numerical findings revealed that most of the performance parameters showed a rise in their values when the oscillator strength was increased without any additional Lorentzian broadening. However, when the broadening was considered, the parameter values dropped implying a counteracting effect. Such outcome indicates that one can tune the optical performance of an excitonic system through its molecular concentration which is not possible in typical plasmonic systems. Moreover, different surface excitonic modes showed different degrees of tunability and equivalency in performance when compared to metals (silver and gold).

In line with our results on various excitonic systems, we can infer that to achieve an efficient performance from these systems, one should aim a molecular concentration corresponds to a large value of f. In practice, however, this approach might incur formation of molecular aggregates at extremely high concentration and thereby, induces challenge to maintain a relatively small value for γ within the broadening tolerance. Such limitation can be mitigated by selecting a molecule possessing strong transition dipole moment with narrow spectral linewidth since then a large f can be achieved with comparatively low molecular concentration while maintaining a small value of γ. Therefore, we can conclude that excitonic systems offer an extra degree of tunability via molecular concentration and are a promising alternative for plasmonics. Our comprehensive study provides key information to develop such alternative systems for organic nanophotonics.

Optical Materials EXPRESS

Appendix

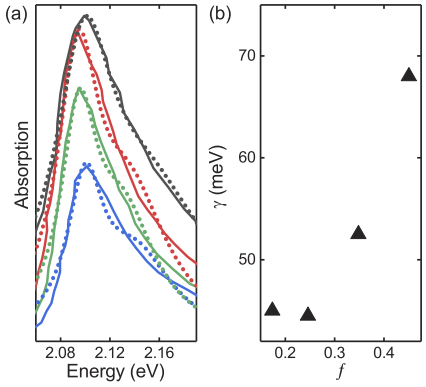

Fig. 7. (a) experimental (solid curves) and fitted (dotted curves) absorption spectra of TDBC J-aggregate thin films with increasing concentration. The experimental (solid curves) spectra are reproduced from Ref. [44]. (b) Lorentz linewidth (γ) as a function of oscillator strength (f) where the values for γ are directly from Ref. [44] while the values for f are obtained by fitting the absorption spectra reported in (a).

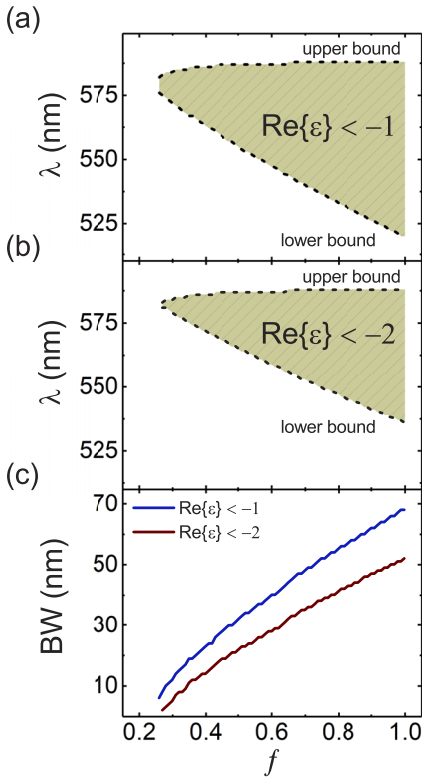

Fig. 8. Negative $Re\{\epsilon\}$ regime of TDBC-PVA system. Wavelength (λ) regions (shaded areas) as a function of oscillator strength (f) where $|Im\{\epsilon\}|<|Re\{\epsilon\}|$ with (a) $Re\{\epsilon\}<-1$ and (b) $Re\{\epsilon\}<-2$. (c) Spectral bandwidth of the surface excitonic modes as a function of f where the bandwidth (BW) is calculated as the difference between the upper and lower bounds shown as black dashed lines in (a)-(b).

Optical Materials EXPRESS

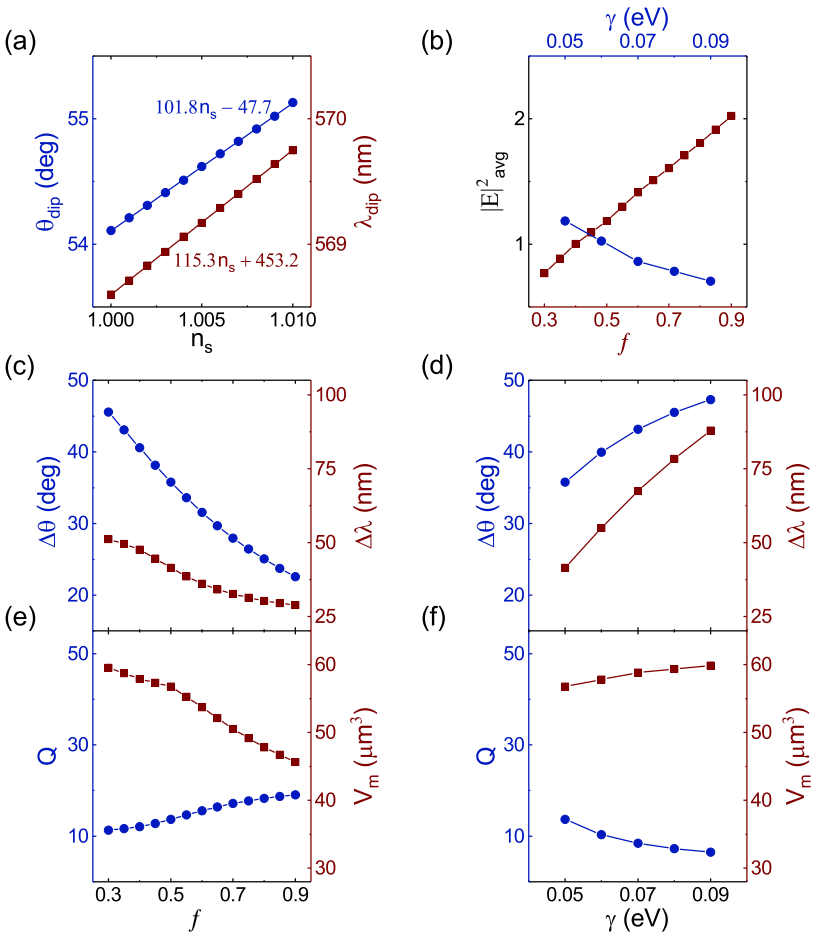

Fig. 9. Properties of the surface exciton polariton (SEP) mode of a 60 nm thick TDBC-PVA film under the Kretschmann configuration. (a) Calibration curves for refractive index (RI) sensing, i.e., reflection minimum (θ_{dip} and λ_{dip}) as a function of the RI of sensing medium (n_s). Linear fits on θ_{dip} and λ_{dip} are performed to calculate the sensitivities as the slopes of the fitted lines. (b) Average near-field intensity enhancement ($|E|^2_{avg}$) as a function of oscillator strength (f) and Lorentz linewidth (γ). Angular ($\Delta\theta$) and spectral ($\Delta\lambda$) full width at half maximum (FWHM) as a function of (c) f, and (d) γ. The quality factor (Q) and mode volume (V_m) as a function of (e) f, and (f) γ. In (b)-(f), f is varied with $\gamma = 0.05$ eV and γ is varied with $f = 0.5$. In (a) and (c)-(f), the blue and red vertical axes correspond to the blue and red curves, respectively. In (b), the blue and red horizontal axes correspond to the blue and red curves, respectively. In all figures, the blue circles and the red squares on the curves of corresponding color depict the discrete data points.

Optical Materials EXPRESS

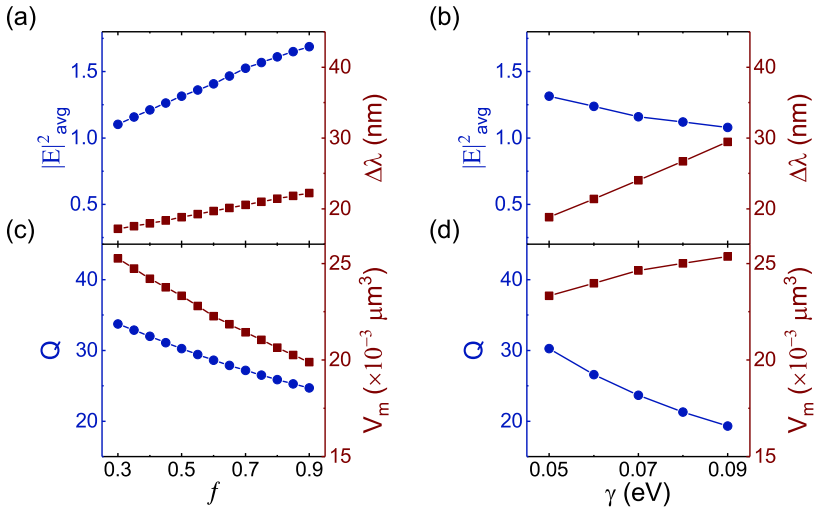

Fig. 10. Properties of the localized surface exciton (LSE) mode of a 100 nm TDBC-PVA nanosphere. Average near-field intensity enhancement ($|E|^2_{avg}$) and spectral full width at half maximum (FWHM) ($\Delta\lambda$) as a function of (a) oscillator strength (f), and (b) Lorentz linewidth (γ). The quality factor (Q) and mode volume (V_m) as a function of (c) f, and (d) γ. In all cases, f is varied with $\gamma = 0.05$ eV and γ is varied with $f = 0.5$. In all figures, the blue and red vertical axes correspond to the blue and red curves, respectively, while the blue circles and the red squares on the curves of corresponding color depict the discrete data points.

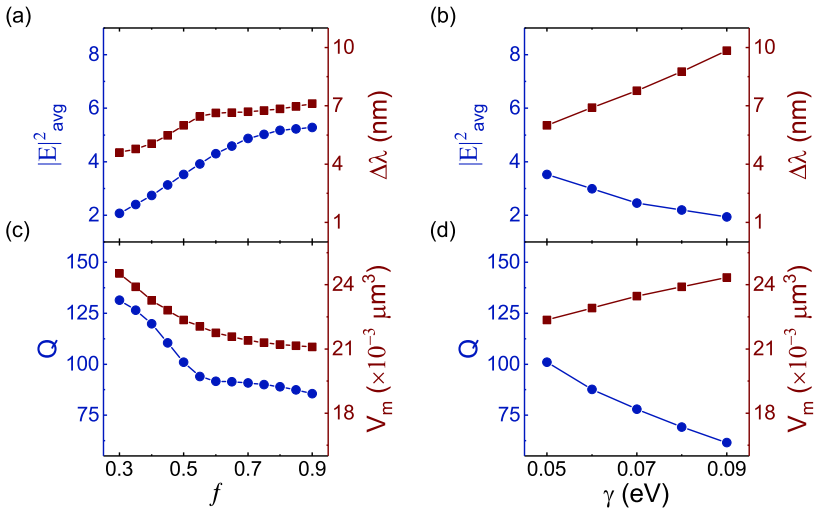

Fig. 11. Properties of the excitonic surface lattice resonance (ESLR) mode of a 400×400 square lattice of 100 nm TDBC-PVA nanospheres with a lattice period of 400 nm. Average near-field intensity enhancement ($|E|^2_{avg}$) and spectral full width at half maximum (FWHM) ($\Delta\lambda$) as a function of (a) oscillator strength (f), and (b) Lorentz linewidth (γ). The quality factor (Q) and mode volume (V_m) as a function of (c) f, and (d) γ. In all cases, f is varied with $\gamma = 0.05$ eV and γ is varied with $f = 0.5$. In all figures, the blue and red vertical axes correspond to the blue and red curves, respectively, while the blue circles and the red squares on the curves of corresponding color depict the discrete data points.

Optical Materials EXPRESS

Table 1. Comparison between - surface plasmon polariton (SPP) and surface exciton polariton (SEP); localized surface plasmon (LSP) and localized surface exciton (LSE); plasmonic surface lattice resonance (PSLR) and excitonic surface lattice resonance (ESLR). The comparison is in terms of - angular (S_θ) and spectral (S_λ) sensitivities; angular (F_θ) and spectral (F_λ) figure of merits; maximum ($|E|^2_{max}$) and average ($|E|^2_{avg}$) of near-field intensity enhancement; quality factor (Q) and mode volume (V_m); Purcell enhancement (Φ_P) and field-confinement (Φ_C).

	Ag	Au	TDBC-PVA
Parameters	**SPP**	**SPP**	**SEP**
S_θ (deg/RIU)	210, 216 [78]	64, 74 [31]	84-109
S_λ (nm/RIU)	2051, 2000 [79]	2711, 1600 [79]	71-184
F_θ (RIU^{-1})	113	29	2-5
F_λ (RIU^{-1})	120	42	1-6
$\lvert E\rvert^2_{max}$	75	65	3-14
$\lvert E\rvert^2_{avg}$	8	8	1-2
Q	26	9	7-19
V_m (μm^3)	29	85	45-60
Φ_P ($\times 10^{-2}\mu$m^{-3})	91	11	11-42
Φ_C ($\times 10^{-2}\mu$m$^{-3/2}$)	19	11	13-15
Parameters	**LSP**	**LSP**	**LSE**
S_λ (nm/RIU)	209, 160 [79]	204, 203 [79]	24-63
F_λ (RIU^{-1})	2	2	1-3
$\lvert E\rvert^2_{max}$	47	17	9-28
$\lvert E\rvert^2_{avg}$	2	2	1-2
Q	4	6	19-34
V_m ($\times 10^{-3}\mu$m^3)	16	25	20-25
Φ_P (μm^{-3})	267	254	761-1335
Φ_C (μm$^{-3/2}$)	8	6	6-7
Parameters	**PSLR**	**PSLR**	**ESLR**
S_λ (nm/RIU)	433, 450 [80]	440, 450 [80]	321-353
F_λ (RIU^{-1})	20	14	35-70
$\lvert E\rvert^2_{max}$	360	128	14-54
$\lvert E\rvert^2_{avg}$	17	8	2-5
Q	29	21	62-132
V_m ($\times 10^{-3}\mu$m^3)	15	12	21-25
Φ_P (μm^{-3})	1973	1707	2528-5359
Φ_C (μm$^{-3/2}$)	8	9	6-7

Funding. Academy of Finland (289947, 323995).

Acknowledgments. The authors would like to thank Academy of Finland under the grant nos. 289947 and 323995 for financial support of this project.

Disclosures. The authors declare no conflicts of interest.

Data availability. Data underlying the results presented in this paper are not publicly available at this time but may be obtained from the authors upon reasonable request.

References

1. S. A. Maier, *Plasmonics: Fundamentals and Applications* (Springer, 2007).

Optical Materials EXPRESS

2. S. Enoch and N. Bonod, *Plasmonics: From Basics to Advanced Topics* (Springer, 2012).
3. T. V. Shahbazyan and M. I. Stockman, *Plasmonics: Theory and Applications* (Springer, 2013).
4. W. L. Barnes, A. Dereux, and T. W. Ebbesen, "Surface plasmon subwavelength optics," Nature **424**(6950), 824–830 (2003).
5. K. A. Willets and R. P. Van Duyne, "Localized surface plasmon resonance spectroscopy and sensing," Annu. Rev. Phys. Chem. **58**(1), 267–297 (2007).
6. V. G. Kravets, A. V. Kabashin, W. L. Barnes, and A. N. Grigorenko, "Plasmonic surface lattice resonances: a review of properties and applications," Chem. Rev. **118**(12), 5912–5951 (2018).
7. J. Homola, *Surface Plasmon Resonance Based Sensors* (Springer, 2006).
8. Y.-T. Long and C. Jing, *Localized Surface Plasmon Resonance Based Nanobiosensors* (Springer, 2014).
9. B. Špačková and J. Homola, "Sensing properties of lattice resonances of 2D metal nanoparticle arrays: an analytical model," Opt. Express **21**(22), 27490–27502 (2013).
10. J. Homola, "Surface plasmon resonance sensors for detection of chemical and biological species," Chem. Rev. **108**(2), 462–493 (2008).
11. P. Offermans, M. C. Schaafsma, S. R. K. Rodriguez, Y. Zhang, M. Crego-Calama, S. H. Brongersma, and J. G. Rivas, "Universal scaling of the figure of merit of plasmonic sensors," ACS Nano **5**(6), 5151–5157 (2011).
12. A. Dutta, T. Nuutinen, K. Alam, A. Matikainen, P. Li, E. Hulkko, J. J. Toppari, H. Lipsanen, and G. Kang, "Fabrication-friendly polarization-sensitive plasmonic grating for optimal surface-enhanced Raman spectroscopy," J. Eur. Opt. Soc.-Rapid Publ. **16**(1), 22 (2020).
13. A. Dutta, K. Alam, T. Nuutinen, E. Hulkko, P. Karvinen, M. Kuittinen, J. J. Toppari, and E. M. Vartiainen, "Influence of Fano resonance on SERS enhancement in Fano-plasmonic oligomers," Opt. Express **27**(21), 30031–30043 (2019).
14. A. Dutta, A. Matikainen, S. Andoh, and T. Nuutinen, "SERS activity of photoreduced silver chloride crystals," AIP Conf. Proc. **2220**, 050004 (2020).
15. F. Laux, N. Bonod, and D. Gérard, "Single emitter fluorescence enhancement with surface lattice resonances," J. Phys. Chem. C **121**(24), 13280–13289 (2017).
16. S. A. Maier, "Plasmonic field enhancement and SERS in the effective mode volume picture," Opt. Express **14**(5), 1957–1964 (2006).
17. Z.-J. Yang, T. J. Antosiewicz, and T. Shegai, "Role of material loss and mode volume of plasmonic nanocavities for strong plasmon-exciton interactions," Opt. Express **24**(18), 20373–20381 (2016).
18. A. Dutta and E. M. Vartiainen, "Spatial localization of hotspots in Fano-resonant plasmonic oligomers for surface-enhanced coherent anti-Stokes Raman scattering," J. Eur. Opt. Soc.-Rapid Publ. **16**(1), 8 (2020).
19. H. Yu, Y. Peng, Y. Yang, and Z.-Y. Li, "Plasmon-enhanced light–matter interactions and applications," npj Comput. Mater. **5**(1), 45 (2019).
20. J.-F. Li, C.-Y. Li, and R. F. Aroca, "Plasmon-enhanced fluorescence spectroscopy," Chem. Soc. Rev. **46**(13), 3962–3979 (2017).
21. J. Langer, J. de Aberasturi, and J. Aizpurua, *et al.*, "Present and future of surface-enhanced Raman scattering," ACS Nano **14**(1), 28–117 (2020).
22. F. Neubrech, C. Huck, K. Weber, A. Pucci, and H. Giessen, "Surface-enhanced infrared spectroscopy using resonant nanoantennas," Chem. Rev. **117**(7), 5110–5145 (2017).
23. S. Baieva, O. Hakamaa, G. Groenhof, T. T. Heikkilä, and J. J. Toppari, "Dynamics of strongly coupled modes between surface plasmon polaritons and photoactive molecules: the effect of the Stokes shift," ACS Photonics **4**(1), 28–37 (2017).
24. A. E. Schlather, N. Large, A. S. Urban, P. Nordlander, and N. J. Halas, "Near-field mediated plexcitonic coupling and giant Rabi splitting in individual metallic dimers," Nano Lett. **13**(7), 3281–3286 (2013).
25. A. I. Väkeväinen, R. J. Moerland, H. T. Rekola, A.-P. Eskelinen, J.-P. Martikainen, D.-H. Kim, and P. Törmä, "Plasmonic surface lattice resonances at the strong coupling regime," Nano Lett. **14**(4), 1721–1727 (2014).
26. L. Gu, J. Livenere, G. Zhu, E. E. Narimanov, and M. A. Noginov, "Quest for organic plasmonics," Appl. Phys. Lett. **103**(2), 021104 (2013).
27. M. J. Gentile, S. Núñez-Sánchez, and W. L. Barnes, "Optical field-enhancement and subwavelength field-confinement using excitonic nanostructures," Nano Lett. **14**(5), 2339–2344 (2014).
28. R. Yu, L. M. Liz-Marzán, and F. J. García de Abajo, "Universal analytical modeling of plasmonic nanoparticles," Chem. Soc. Rev. **46**(22), 6710–6724 (2017).
29. D. Barchiesi and T. Grosges, "Fitting the optical constants of gold, silver, chromium, titanium, and aluminum in the visible bandwidth," J. Nanophotonics **8**(1), 083097 (2014).
30. K. Takatori, T. Okamoto, K. Ishibashi, and R. Micheletto, "Surface exciton polaritons supported by a J-aggregate-dye/air interface at room temperature," Opt. Lett. **42**(19), 3876–3879 (2017).
31. Y. Xu, L. Wu, and L. K. Ang, "Surface exciton polaritons: a promising mechanism for refractive-index sensing," Phys. Rev. Appl. **12**(2), 024029 (2019).
32. M. J. Gentile, S. A. R. Horsley, and W. L. Barnes, "Localized exciton–polariton modes in dye-doped nanospheres: a quantum approach," J. Opt. **18**(1), 015001 (2016).
33. M. J. Gentile and W. L. Barnes, "Hybridised exciton–polariton resonances in core–shell nanoparticles," J. Opt. **19**(3), 035003 (2017).

Optical Materials EXPRESS

34. A. D. Humphrey, M. J. Gentile, and W. L. Barnes, "Excitonic surface lattice resonances," J. Opt. **18**(8), 085004 (2016).
35. A. Cacciola, C. Triolo, O. D. Stefano, A. Genco, M. Mazzeo, R. Saija, S. Patanè, and S. Savasta, "Subdiffraction light concentration by J-aggregate nanostructures," ACS Photonics **2**(7), 971–979 (2015).
36. S. Baieva, T. K. Hakala, and J. J. Toppari, "Strong coupling between surface plasmon polaritons and sulforhodamine 101 dye," Nanoscale Res. Lett. **7**(1), 191 (2012).
37. A. Dutta, V. Tiainen, H. A. Qureshi, L. Duarte, and J. J. Toppari, "Modeling optical constants from the absorption of organic thin films using a modified Lorentz oscillator model," Opt. Mater. Express **12**(7), 2855–2869 (2022).
38. B. Valeur and M. N. Berberan-Santos, *Molecular Fluorescence: Principles and Applications* (Wiley-VCH, 2012).
39. A. Canales, D. G. Baranov, T. J. Antosiewicz, and T. Shegai, "Abundance of cavity-free polaritonic states in resonant materials and nanostructures," J. Chem. Phys. **154**(2), 024701 (2021).
40. W. J. Tan, P. A. Thomas, I. J. Luxmoore, and W. L. Barnes, "Single vs double anti-crossing in the strong coupling between surface plasmons and molecular excitons," J. Chem. Phys. **154**(2), 024704 (2021).
41. G. Zengin, G. Johansson, P. Johansson, T. J. Antosiewicz, M. Käll, and T. Shegai, "Approaching the strong coupling limit in single plasmonic nanorods interacting with J-aggregates," Sci. Rep. **3**(1), 3074 (2013).
42. D. M. Coles, P. Michetti, C. Clark, A. M. Adawi, and D. G. Lidzey, "Temperature dependence of the upper-branch polariton population in an organic semiconductor microcavity," Phys. Rev. B **84**(20), 205214 (2011).
43. K. Das, J. Dey, M. S. Verma, M. Kumar, and M. Chandra, "Probing the role of oscillator strength and charge of exciton forming molecular J-aggregates in controlling nanoscale plasmon–exciton interactions," Phys. Chem. Chem. Phys. **22**(36), 20499–20506 (2020).
44. M. S. Bradley, J. R. Tischler, and V. Bulović, "Layer-by-layer J-aggregate thin films with a peak absorption constant of 10^6 cm^{-1}," Adv. Mater. **17**(15), 1881–1886 (2005).
45. T. G. Mackay and A. Lakhtakia, *The Transfer-Matrix Method in Electromagnetics and Optics* (Morgan and Claypool, 2020).
46. K. J. Pascoe, *Reflectivity and Transmissivity Through Layered, Lossy Media: A User-Friendly Approach* (Wright Patterson Air Force Base, 2001).
47. K. Sayood, *Learning Programming Using MATLAB* (Morgan and Claypool, 2006).
48. https://www.mathworks.com/products/matlab.html.
49. L. C. Oliveira, A. M. N. Lima, C. Thirstrup, and H. F. Neff, *Surface Plasmon Resonance Sensors* (Springer, 2019).
50. K. Takagi, S. V. Nair, R. Watanabe, K. Seto, T. Kobayashi, and E. Tokunaga, "Surface plasmon polariton resonance of gold, silver, and copper studied in the Kretschmann geometry: dependence on wavelength, angle of incidence, and film thickness," J. Phys. Soc. Jpn. **86**(12), 124721 (2017).
51. I. Chambouleyron and J. M. Martínez, "Optical properties of dielectric and semiconductor thin films," in *Handbook of Thin Films*, H. S. Nalwa, ed. (Academic Press, 2002).
52. S. D. Gedney, *Introduction to the Finite-Difference Time-Domain (FDTD) Method for Electromagnetics* (Morgan and Claypool, 2011).
53. https://www.ansys.com/products/photonics/fdtd.
54. K. J. Vahala, "Optical microcavities," Nature **424**(6950), 839–846 (2003).
55. A. Dutta, V. Tiainen, and J. J. Toppari, "Optimizing geometry of low-Q all-metal Fabry-Pérot microcavity for fluorescence spectroscopy," IOPSciNotes **2**(1), 015205 (2021).
56. M. S. Rider and W. L. Barnes, "Something from nothing: linking molecules with virtual light," Contemp. Phys. **62**(4), 217–232 (2021).
57. https://optics.ansys.com/hc/en-us/articles/360034395374.
58. C. F. Bohren and D. R. Huffman, *Absorption and Scattering of Light by Small Particles* (Wiley-VCH, 1998).
59. G. Baffou, *Thermoplasmonics: Heating Metal Nanoparticles Using Light* (Cambridge University Press, 2017).
60. M. Quinten, *Optical Properties of Nanoparticle Systems: Mie and Beyond* (Wiley-VCH, 2011).
61. A. Trügler, *Optical Properties of Metallic Nanoparticles* (Springer, 2016).
62. K. Travis and J. Guck, "Scattering from single nanoparticles: Mie theory revisited," Biophys. Rev. Lett. **01**(02), 179–207 (2006).
63. A. Dutta, V. Tiainen, and J. J. Toppari, "Numerical study on the limit of quasi-static approximation for plasmonic nanosphere," AIP Conf. Proc. **2220**, 050012 (2020).
64. W. L. Barnes, "Particle plasmons: why shape matters," Am. J. Phys. **84**(8), 593–601 (2016).
65. S. T. Holder, C. Estévez-Varela, I. Pastoriza-Santos, M. Lopez-Garcia, R. Oulton, and S. Núñez-Sánchez, "Bio-inspired building blocks for all-organic metamaterials from visible to near-infrared," Nanophotonics **12**(2), 307–318 (2023).
66. S. Chen, E. S. H. Kang, M. S. Chaharsoughi, V. Stanishev, P. Kühne, H. Sun, C. Wang, M. Fahlman, S. Fabiano, V. Darakchieva, and M. P. Jonsson, "Conductive polymer nanoantennas for dynamic organic plasmonics," Nat. Nanotechnol. **15**(1), 35–40 (2020).
67. D. Khlopin, F. Laux, W. P. Wardley, J. Martin, G. A. Wurtz, J. Plain, N. Bonod, A. V. Zayats, W. Dickson, and D. Gérard, "Lattice modes and plasmonic linewidth engineering in gold and aluminum nanoparticle arrays," J. Opt. Soc. Am. B **34**(3), 691–700 (2017).
68. B. Auguié, X. M. Bendaña, W. L. Barnes, and F. J. García de Abajo, "Diffractive arrays of gold nanoparticles near an interface: critical role of the substrate," Phys. Rev. B **82**(15), 155447 (2010).

Optical Materials EXPRESS

69. S. Zou, N. Janel, and G. C. Schatz, "Silver nanoparticle array structures that produce remarkably narrow plasmon lineshapes," J. Chem. Phys. **120**(23), 10871–10875 (2004).
70. S. Zou and G. C. Schatz, "Narrow plasmonic/photonic extinction and scattering line shapes for one and two dimensional silver nanoparticle arrays," J. Chem. Phys. **121**(24), 12606–12612 (2004).
71. C. Cherqui, M. R. Bourgeois, D. Wang, and G. C. Schatz, "Plasmonic surface lattice resonances: theory and computation," Acc. Chem. Res. **52**(9), 2548–2558 (2019).
72. R. Adato, A. A. Yanik, C.-H. Wu, G. Shvets, and H. Altug, "Radiative engineering of plasmon lifetimes in embedded nanoantenna arrays," Opt. Express **18**(5), 4526–4537 (2010).
73. B. Auguié and W. L. Barnes, "Collective resonances in gold nanoparticle arrays," Phys. Rev. Lett. **101**(14), 143902 (2008).
74. A. D. Humphrey and W. L. Barnes, "Plasmonic surface lattice resonances on arrays of different lattice symmetry," Phys. Rev. B **90**(7), 075404 (2014).
75. A. D. Humphrey and W. L. Barnes, "Plasmonic surface lattice resonances in arrays of metallic nanoparticle dimers," J. Opt. **18**(3), 035005 (2016).
76. S. Zou and G. C. Schatz, "Theoretical studies of plasmon resonances in one-dimensional nanoparticle chains: narrow lineshapes with tunable widths," Nanotechnology **17**(11), 2813–2820 (2006).
77. P. B. Johnson and R. W. Christy, "Optical constants of the noble metals," Phys. Rev. B **6**(12), 4370–4379 (1972).
78. A. H. M. Almawgani, S. K. Awasthi, A. Mehaney, G. A. Ali, H. A. Elsayed, H. Sayed, and A. M. Ahmed, "A theoretical approach for a new design of an ultrasensitive angular plasmonic chemical sensor using black phosphorus and aluminum oxide architecture," RSC Adv. **13**(24), 16154–16164 (2023).
79. Y. Xu, P. Bai, X. Zhou, Y. Akimov, C. E. Png, L.-K. Ang, W. Knoll, and L. Wu, "Optical refractive index sensors with plasmonic and photonic structures: promising and inconvenient truth," Adv. Opt. Mater. **7**(9), 1801433 (2019).
80. A. Minopoli, A. Acunzo, B. D. Ventura, and R. Velotta, "Nanostructured surfaces as plasmonic biosensors: a review," Adv. Mater. Interfaces **9**(2), 2101133 (2022).